THE JOURNAL OF PHYSICAL CHEMISTRY C

Article

pubs.acs.org/JPCC

Electron-Induced Surface Reactions of η^3-Allyl Ruthenium Tricarbonyl Bromide [(η^3-C_3H_5)Ru(CO)$_3$Br]: Contrasting the Behavior of Different Ligands

Julie A. Spencer,[†] Joseph A. Brannaka,[‡] Michael Barclay,[†] Lisa McElwee-White,[‡] and D. Howard Fairbrother*,[†]

[†]Department of Chemistry, Johns Hopkins University, Baltimore, Maryland 21218, United States

[‡]Department of Chemistry, University of Florida, Gainesville, Florida 32611-7200, United States

S *Supporting Information*

ABSTRACT: Toward the goal of better understanding the elementary steps involved in the electron beam-induced deposition (EBID) of organometallic precursors, the present study is aimed at understanding the sequence of electron-stimulated reactions of surface-bound η^3-allyl ruthenium tricarbonyl bromide [(η^3-C_3H_5)Ru(CO)$_3$Br], an organometallic complex with three different ligands: carbonyl (CO), halide (Br), and η^3-allyl (η^3-C_3H_5). X-ray photoelectron spectroscopy and mass spectrometry were used in situ to probe the effects of 500 eV electrons on nanometer scale films of [(η^3-C_3H_5)Ru(CO)$_3$Br]. Initially, electron irradiation decomposes the precursor, reducing the central Ru atom and causing the ejection of CO ligands into the gas phase. Experimental evidence points to the inability of electron irradiation to remove the carbon atoms of the η^3-allyl (η^3-C_3H_5) ligand from the resulting EBID deposits. Although the Br atoms are not labile in the initial molecular decomposition step, they are removed from the film after exposure to higher electron doses as a result of a slower, electron-stimulated desorption process. Comparative studies with [(η^3-C_3H_5)Ru(CO)$_3$Cl] reveal that the identity of the halogen does not influence the elementary reaction steps involved in the decomposition process. Collectively, results from these studies suggest that sufficiently volatile organometallic precursors with a small number of carbonyl and halide ligands could be used to generate deposits in EBID with significantly higher metal concentrations (and correspondingly lower levels of organic contamination) compared to existing EBID precursors.

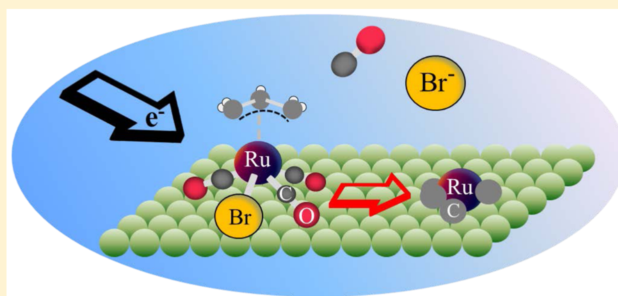

I. INTRODUCTION

Electron beam-induced deposition (EBID) is a single step, vacuum-based, lithographic strategy typically performed in a modified scanning electron microscope (SEM) that uses a focused electron beam to create metal-containing nanostructures from the deposition of organometallic precursors.[1−4] Deposition occurs as a result of electron-stimulated decomposition of the molecular precursor to form nonvolatile, metal-containing fragments (the deposit).[3,4] The inherent flexibility of the electron beam allows EBID to produce an almost unlimited array of three-dimensional nanostructures where the size and shape can be accurately controlled and varied; nanostructures <1 nm in diameter have been reported.[5,6] There are numerous potential applications of EBID, particularly in the area of prototyping nanostructures; current commercial uses include the repair of extreme ultraviolet light lithography (EUVL) masks[7−9] and the production of custom tips for scanning tunneling[10] and atomic force microscopies.[11,12]

For the full potential of EBID to be realized, however, one major challenge relating to the high levels of organic contamination found in EBID nanostructures must be overcome.[3,13] These impurities negatively impact properties such as resistivity and conductivity, limiting the current applications of EBID nanostructures.[3,4,14] The organic contamination can be traced back in large part to the structure, chemical composition, and decomposition mechanisms of existing EBID precursors, which have typically been designed for thermal deposition processes, such as chemical vapor deposition (CVD),[3,13] rather than electron-stimulated processes, such as EBID. A better understanding of the fundamental bond-breaking steps involved in EBID would help to elucidate the mechanisms of organic contamination and the fate of different ligands, providing knowledge that could be used in the design of precursors optimized specifically for EBID.[15] Indeed, there is a general need for more fundamental physical and chemical information on the various processes involved in EBID. This has provided the motivation to understand the electron interactions with EBID precursors in the gas phase,[16−20] as well as adsorption energies, surface

Received: April 20, 2015
Revised: June 4, 2015
Published: June 8, 2015

 © 2015 American Chemical Society

DOI: 10.1021/acs.jpcc.5b03775
J. Phys. Chem. C 2015, 119, 15349−15359

dynamics,[21,22] and reaction cross sections[23] of precursor molecules adsorbed on surfaces.

In typical EBID, it is very difficult to identify the sequence of events that accompany deposition, including bond-breaking and desorption processes, due to the steady state deposition conditions, the extremely large fluxes of electrons used, the presence of additional processes, such as diffusion, and the effects of contaminant gases typically present in electron microscopes.[3,4] To gain more fundamental insights into the EBID process, we have employed an ultrahigh vacuum (UHV) surface science approach to study the reactions of EBID precursors under electron irradiation. In contrast to traditional EBID studies, the UHV surface science approach examines the effects of electron irradiation on nanometer-thick films of precursor molecules adsorbed onto chemically inert substrates at low temperatures.[24−29] This experimental approach has also recently been used to examine electron-induced reactions of ligands present in EBID precursors.[30]

In our experimental apparatus, X-ray photoelectron spectroscopy (XPS) is used in situ to follow changes in bonding environment and surface composition of the various elements contained in the precursor molecule, and mass spectrometry (MS) provides complementary information on the volatile species ejected from the film as a result of electron irradiation. Both XPS and MS can be acquired as a function of electron dose, helping to elucidate the sequence of electron-stimulated processes. Use of a low temperature (<200 K) UHV environment (P_{base} $<5 \times 10^{-9}$ Torr) also simplifies data interpretation because it largely eliminates complicating effects from diffusion and adsorbed contaminants (e.g., water and hydrocarbons). Additionally, the low background pressure allows identification of gas phase products produced during electron beam irradiation; this information is not available in typical EBID experiments due to both the presence of a constant partial pressure of precursor molecules during deposition and the higher base pressure.[26]

Previous UHV surface science studies[24,25,27,28,31−34] have revealed that the electron beam-induced reactions of organometallic compounds typically occur in two relatively discrete steps.[24,26,27] In the first step, a transiently adsorbed precursor undergoes an electron-stimulated reaction that results in ligand desorption and leaves behind a partially decomposed surface-bound intermediate. Continued electron beam irradiation (always present in EBID due to the large electron fluxes involved) results predominantly in decomposition of the ligands contained in the surface-bound intermediate.[25] It is this second step that we believe is the primary cause of the organic contamination observed in EBID nanostructures. For example, when adsorbed $W(CO)_6$ (an EBID precursor) is irradiated with electrons, some CO ligands are initially desorbed into the gas phase and a partially decarbonylated surface-bound intermediate, $W_x(CO)_y$, remains behind.[32] Continued electron irradiation of these surface-bound intermediates, however, causes decomposition of the remaining CO ligands, which results in oxidized tungsten atoms encased in a carbonaceous matrix.

The specific goal of the present study is to compare and contrast the behavior of different ligands that are often present in organometallic precursors used in EBID. On the basis of our previous studies,[24,25,27,28,31−34] the fate of ligands in an organometallic precursor undergoing EBID can be expected to fall into two general categories: (1) the ligands are ejected and pumped away into the gas phase as the precursor decomposes; or (2) the ligands are decomposed by electron beam irradiation following precursor decomposition and become incorporated into the deposit, contributing to contamination. As a vehicle to elucidate the behavior of different ligands, we have studied the electron-stimulated reactions of surface-bound η^3-allyl ruthenium tricarbonyl bromide [(η^3-C_3H_5)Ru$(CO)_3$Br)] and, to a lesser extent, η^3-allyl ruthenium tricarbonyl chloride [η^3-C_3H_5)Ru$(CO)_3$Cl)]. These complexes provide the opportunity to simultaneously evaluate the behavior of three different types of ligands in the same coordination sphere: carbonyl (CO), η^3-allyl (η^3-C_3H_5), and halides (Br, Cl). Although the bulk of the studies reported in this investigation were UHV surface science studies, to provide a more direct comparison to typical EBID studies, we also created deposits using [(η^3-C_3H_5)Ru$(CO)_3$Br)] and [η^3-C_3H_5)Ru$(CO)_3$Cl)] under steady state deposition conditions in an Auger electron spectrometer, and the chemical composition of the deposits and the effect of post-deposition electron beam processing were studied.

Previous work has indicated that, under electron irradiation, carbonyl groups are susceptible to both ejection as intact molecules and decomposition depending on the number of attached CO groups.[31,32] The η^3-allyl (η^3-C_3H_5) is a polyhapto unsaturated hydrocarbon ligand and is less strongly bound than the π-facial carbon-bonded cyclopentadienyl (η^5-C_5H_5, Cp) ligand, which has been shown to be a poor leaving group under electron irradiation with the carbon atoms being retained in the metal-containing carbonaceous matrix that forms during EBID.[28] Although the η^3-allyl ligand could reasonably be predicted to behave similarly to the cyclopentadienyl (Cp) ligand, the lower hapticity (and resulting weaker metal−ligand bonding) raised the question of whether it could be removed under EBID conditions. The fate of halides directly bonded to the metal center has not been explicitly explored in EBID.[3,4]

II. EXPERIMENTAL SECTION

An ultrahigh vacuum (UHV) surface science chamber was used to study the effects of electron irradiation on nanometer-thick films of η^3-allyl ruthenium tricarbonyl bromide [(η^3-C_3H_5)Ru$(CO)_3$Br] and, for a few comparative experiments, η^3-allyl ruthenium tricarbonyl chloride [(η^3-C_3H_5)Ru$(CO)_3$Cl]. The UHV chamber is equipped with X-ray photoelectron spectroscopy (XPS) and mass spectrometry (MS) and, during experiments, operates at a base pressure of $<5 \times 10^{-9}$ Torr. Details of the chamber and its analytical capabilities, including the manipulator, electron gun, and sample cleaning protocols can be found in previous publications.[25,27,28]

Precursors. η^3-Allyl ruthenium tricarbonyl bromide [(η^3-C_3H_5)Ru$(CO)_3$Br] and η^3-allyl ruthenium tricarbonyl chloride [(η^3-C_3H_5)Ru$(CO)_3$Cl] are both stable white solids at standard temperature and pressure. Prior to deposition, the precursor was added to a glass finger, which was coupled to the UHV chamber via a stainless steel tubing manifold and a UHV compatible leak valve. The gas manifold and glass finger were then evacuated by a mechanical pump into the mTorr pressure regime. Both compounds possessed sufficient vapor pressure to be dosed successfully at room temperature, although the chloride analogue was significantly more volatile and therefore easier to dose. During the course of the experiments, it was also found that by heating the precursor in the glass finger to ∼40 °C during film deposition the co-adsorption of a small amount of unwanted hydrocarbons/adventitious carbon could be significantly reduced (see Figure S1, Supporting Information).

DOI: 10.1021/acs.jpcc.5b03775
J. Phys. Chem. C 2015, 119, 15349−15359

Synthesis of η^3-Allyl Ruthenium Tricarbonyl Bromide [(η^3-C_3H_5)Ru(CO)$_3$Br]. [(η^3-C_3H_5)Ru(CO)$_3$Br] was synthesized using a modified literature procedure.[35] $Ru_3(CO)_{12}$ (1.0073 g, 1.5756 mmol, Sigma-Aldrich) was added to 20 mL of 2,2,4-trimethylpentane (Sigma-Aldrich) under nitrogen. Allyl bromide (5.0 mL, 58 mmol, Sigma-Aldrich) was added, and the mixture was immediately refluxed. Upon heating, the $Ru_3(CO)_{12}$ dissolved, turning the solution deep red. After 20 minutes of reflux, the solution turned yellow, and the solvent was removed in vacuo. The resulting yellow solid was sublimed at 30 °C and 80 mTorr to yield a white solid (1.2907 g, 89%). ^{1}H NMR ($CDCl_3$, 300 MHz): δ 3.14 (dt, 2H, J = 13.1, 1.0 Hz), 4.11 (dt, 2H, J = 7.8, 1.1 Hz), 5.17 (tt, 1H, J = 13.1, 7.8 Hz). The product was identified by comparison to literature data[35] and supported by attenuated total reflectance-infrared spectroscopy (ATR-IR) (see Figure S2, Supporting Information).

Synthesis of η^3-Allyl Ruthenium Tricarbonyl Chloride [(η^3-C_3H_5)Ru(CO)$_3$Cl]. [(η^3-C_3H_5)Ru(CO)$_3$Cl] was synthesized using a modified literature procedure.[35] $Ru_3(CO)_{12}$ (0.9799 g, 1.533 mmol, Sigma-Aldrich) was added to 20 mL of 2,2,4-trimethylpentane (Sigma-Aldrich) under nitrogen. Allyl chloride (4.6 mL, 56 mmol, Sigma-Aldrich) was added, and the mixture was immediately refluxed. Upon heating, the $Ru_3(CO)_{12}$ dissolved, turning the solution deep red. After 50 minutes of reflux, the solution turned yellow, and the solvent was removed in vacuo. The resulting yellow solid was sublimed at 30 °C and 90 mTorr to yield a white solid (0.7967 g, 66%). ^{1}H NMR ($CDCl_3$, 300 MHz): δ 2.96 (dd, 2H, J =13.3, 1.5 Hz), 4.19 (dd, 2H, J =7.9, 1.5 Hz), 5.30 (ttd, 1H, J =13.3, 7.9, 1.5 Hz). The product was identified by comparison to literature data[35] and supported by ATR-IR (see Figure S2, Supporting Information).

Substrates. The majority of the XPS and MS experiments were performed on an amorphous carbon (a:C) substrate with a small number conducted on a polycrystalline Au substrate. Consistent with previous studies,[25,31−33] the chemical identity of the substrate did not impact the low temperature, electron induced reactions of [(η^3-C_3H_5)Ru(CO)$_3$Br] or [(η^3-C_3H_5)-Ru(CO)$_3$Cl] in terms of the XPS or MS results.

Creating Films. *(i). UHV Conditions.* Nanometer scale films of [(η^3-C_3H_5)Ru(CO)$_3$Br] and [(η^3-C_3H_5)Ru(CO)$_3$Cl] were created by leaking the precursor through a UHV-compatible leak valve onto a cooled substrate. A substrate temperature of −168 °C was necessary to achieve molecular adsorption of the precursors under UHV conditions. Average film thicknesses were determined by measuring the attenuation of the substrate XPS photoelectrons (Au(4f) or C(1s)) upon film deposition.

(ii). In the Auger Electron Spectrometer (AES). Films were created by leaking [(η^3-C_3H_5)Ru(CO)$_3$Br] or [(η^3-C_3H_5)Ru-(CO)$_3$Cl] into the chamber through a UHV-compatible leak valve coupled to a directional doser to create a constant partial pressure of precursor molecules at the Ag substrate surface during deposition. While dosing, the electron beam was rastered across the surface to produce rectangular structures with lengths on the order of several hundred microns. The films were made with a substrate current of 700 nA, incident beam energy of 3 keV, and a partial pressure of 5×10^{-7} Torr with a 90 min deposition time.

III. RESULTS

Figure 1 shows how the C(1s)/Ru(3d), O(1s), and Br(3d) XPS regions of 1−2 nm thick films of [(η^3-C_3H_5)Ru(CO)$_3$Br] adsorbed onto (a:C) substrates evolve as a function of increasing electron dose. To determine the effect that X-ray irradiation has on the [(η^3-C_3H_5)Ru(CO)$_3$Br] films, separate control studies were performed on both a:C (Figure S3, Supporting Information) and Au (Figure S4, Supporting Information) substrates. A comparison of the results shown in Figure 1 and Figures S3 and S4, Supporting Information, demonstrate that 500 eV incident electrons and XPS irradiation have similar effects on the C(1s)/Ru(3d), O(1s), and Br(3d) regions. This is almost certainly a consequence of the transformations being driven by the low energy secondary electrons produced by the interactions of the X-ray beam or the 500 eV incident electron beam with the substrate. To minimize the effect of X-ray irradiation, we exposed each film to X-ray irradiation only twice: once to verify the chemical composition and thickness of the as-deposited film, and then after one controlled and quantified electron dose from the electron gun. Analysis of Figure S4 in the Supporting Information reveals that for [(η^3-C_3H_5)Ru(CO)$_3$Br] adsorbed on a:C substrates, the X-ray irradiation time required for these two XPS to be acquired produces the same effect as an electron dose of $\sim 9.36 \times 10^{14}$ e^-/cm^2. This "additional" electron dose due to XPS acquisition has been factored in to all of the XPS data shown in Figures 1−4, 6, and 7. In practice, however, for all but the shortest electron exposures ($\leq 1.87 \times 10^{15}$ e^-/cm^2), the changes observed by XPS are determined almost exclusively by the 500 eV electron beam.

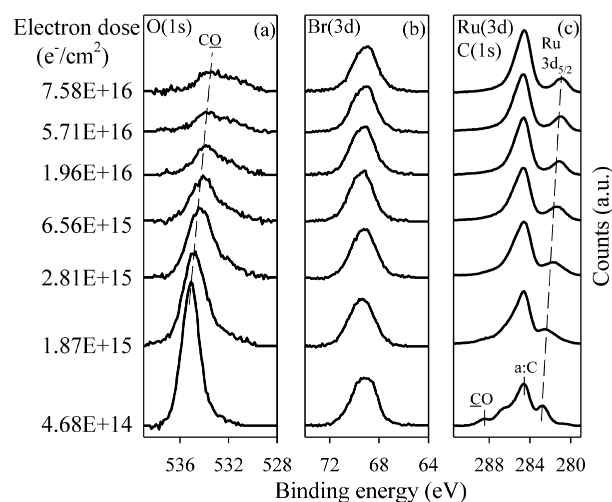

Figure 1. Evolution of the (a) O(1s), (b) Br(3d), and (c) Ru(3d)/C(1s) XP regions for 1−2 nm thick films of [(η^3-C_3H_5)Ru(CO)$_3$Br] exposed to electron doses of $\leq 7.58 \times 10^{16}$ e^-/cm^2. Spectra were normalized to account for slight differences in film thickness.

Figure 1a shows that, prior to electron irradiation, the O(1s) region is composed of a single peak centered at 535.1 eV, typical of the binding energy for a CO species.[36] Upon electron irradiation, the O(1s) peak decreases in intensity, broadens, and ultimately decreases to a lower binding energy. After an electron dose of 7.58×10^{16} e^-/cm^2, the oxygen peak area is <20% of its initial value, whereas the binding energy is decreased by 1.5 eV. Prior to electron irradiation, the Br(3d) region (Figure 1b) is composed of a single asymmetric Br($3d_{5/2,3/2}$) peak with a maximum at 69.2 eV. Electron doses of $\leq 7.58 \times 10^{16}$ e^-/cm^2 are seen to have little effect on the Br(3d) peak area or position. Figure 1c shows changes in the Ru(3d) and C(1s) peaks as a consequence of electron irradiation. Both of these transitions lie between 280 and 290

DOI: 10.1021/acs.jpcc.5b03775
J. Phys. Chem. C 2015, 119, 15349−15359

eV, making spectral deconvolution difficult, particularly on an a:C substrate (peak centered at 284.6 eV[36]). However, Figure 1c does show that upon $(\eta^3\text{-}C_3H_5)Ru(CO)_3Br$ adsorption a Ru $3d_{5/2}$ peak appears at 282.8 eV along with a smaller peak at 288.5 eV, the latter corresponding to the C(1s) peak for an adsorbed CO species. After an electron dose of 7.58×10^{16} e^-/cm^2, the CO peak has disappeared, and the Ru $3d_{5/2}$ binding energy decreased to 280.9 eV.

Figure 2 presents the fractional changes in the O(1s) and Br(3d) peak areas relative to values measured prior to electron beam irradiation, as well as the Ru $3d_{5/2}$ binding energy, each plotted as a function of electron dose. Of note, the O(1s) and Br(3d) species behave in markedly different fashions. As the precursor film is irradiated, the O(1s) peak area decreases significantly at a rate that closely correlates with the decrease in Ru $3d_{5/2}$ binding energy. In contrast, electron irradiation has minimal effect on the Br(3d) area.

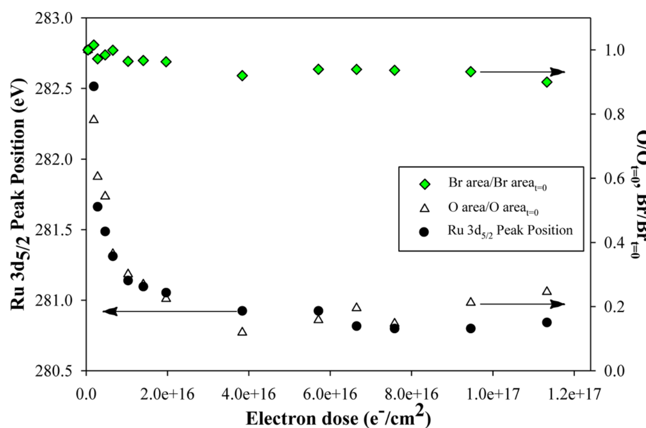

Figure 2. Changes in the fractional coverage (right-hand axis) of oxygen (open triangles) and bromine (filled diamonds) and (left-hand axis) Ru $3d_{5/2}$ peak position (filled circles) for 1−2 nm $[(\eta^3\text{-}C_3H_5)Ru(CO)_3Br]$ films; each is plotted as a function of electron dose (electron doses <1.2×10^{17} e^-/cm^2), and all determined by XPS.

Figure 1c shows how the presence of a dominant a:C substrate peak at 284.6 eV prevents a detailed analysis of the effect of electron irradiation on the Ru(3d) and C(1s) binding energies and signal intensities for $[(\eta^3\text{-}C_3H_5)Ru(CO)_3Br]$ molecules. To circumvent this issue, we performed analogous experiments on a Au substrate (Figure 3). These experiments revealed that, along with the precursor, a small amount of unwanted hydrocarbon adsorption was observed. This was overcome by simply heating the precursor to 40 °C to increase the partial pressure of $(\eta^3\text{-}C_3H_5)Ru(CO)_3Br$ (Figure S1). Prior to electron irradiation, the Ru(3d)/C(1s) spectral envelope can be fit with four peaks: a peak centered at 288.8 eV, corresponding to the CO species, a peak centered at 285.1 eV, corresponding to an adsorbed allyl $(\eta^3\text{-}C_3H_5)$ species, and peaks at 286.8 and 282.8 eV, corresponding to the Ru $3d_{3/2}$ and $3d_{5/2}$ transitions, respectively.[36] Area analysis reveals that the CO and $\eta^3\text{-}C_3H_5$ peak areas prior to electron irradiation are roughly equal in intensity, consistent with the chemical composition of the precursor. Further evidence for the adsorption of molecularly intact $[(\eta^3\text{-}C_3H_5)Ru(CO)_3Br]$ comes from the measured O:Br stoichiometry, which can be determined with reasonable accuracy by XPS (see Figure 1). Thus, analysis of the film shown in Figure 1 prior to electron exposure reveals an O:Br ratio of 3.5:1, which is within experimental error of the 3:1 molecular stoichiometry. The lack of molecular decomposition upon adsorption at −168 °C is consistent with the presence of two C(1s) peaks of approximately equal intensity as well as the single O(1s) peak and well-defined $Br(3d_{5/2}/3d_{3/2})$ doublet (see Figure 1). After an electron dose of 1.13×10^{17} e^-/cm^2, Figure 3 shows that the CO peak has all but disappeared, whereas the peak at 285.1 eV persists and possibly increases slightly in intensity. A more quantitative analysis of Figure 3 is not possible or merited,

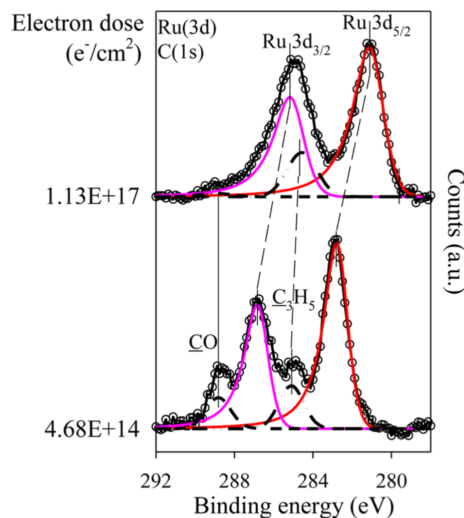

Figure 3. Evolution of the Ru(3d)/C(1s) XP region for a 1.4 nm-thick film of $[(\eta^3\text{-}C_3H_5)Ru(CO)_3Br]$ exposed to an electron dose of 1.13×10^{17} e^-/cm^2. The film was adsorbed onto a Au substrate at −168 °C.

however, due to the difficulty in obtaining an unambiguous spectral fit in the presence of the overlapping, larger, and asymmetric Ru peaks. Analysis of the Ru $3d_{5/2}$ peak, which is sufficiently well separated from other overlapping Ru and C peaks, indicates that it decreases in binding energy by ∼1.7 eV as a result of electron irradiation, which is qualitatively consistent with the observations in Figure 1c.

Figure 4 illustrates that, although comparatively small electron doses (<1.13×10^{17} e^-/cm^2; see Figures 1 and 2) caused minimal loss of Br, significantly larger (∼2 orders of magnitude) electron doses actually caused the majority of the Br species to desorb. Because of the irradiation time necessary to achieve these larger electron doses (over 50 hours), they were conducted at room temperature after $[(\eta^3\text{-}C_3H_5)Ru(CO)_3Br]$ films had initially been exposed to an electron dose of 1.13×10^{17} e^-/cm^2 at −168 °C, which is a dose that is sufficient to decompose all of the parent molecules (see Discussion). When the temperature of these electron-irradiated films increased from −168 °C to room temperature, there were no changes in each film's chemical composition or binding energies of the various elements, indicating that the film created by electron irradiation of adsorbed $[(\eta^3\text{-}C_3H_5)Ru(CO)_3Br]$ molecules remained stable and chemically unaltered. Figure 4a shows evolution of the Br(3d) XPS region of the film. For comparatively small electron doses (≤1.13×10^{17} e^-/cm^2), the Br(3d) region contains an asymmetric peak centered at 69.2 eV, which decreases in intensity and broadens slightly as the electron dose increases, although the binding energy remains unchanged. After an electron dose of 1.24×10^{19} e^-/cm^2, the Br peak area has been reduced to ∼20% of its initial value. These larger electron doses also caused a systematic decrease in

DOI: 10.1021/acs.jpcc.5b03775
J. Phys. Chem. C 2015, 119, 15349−15359

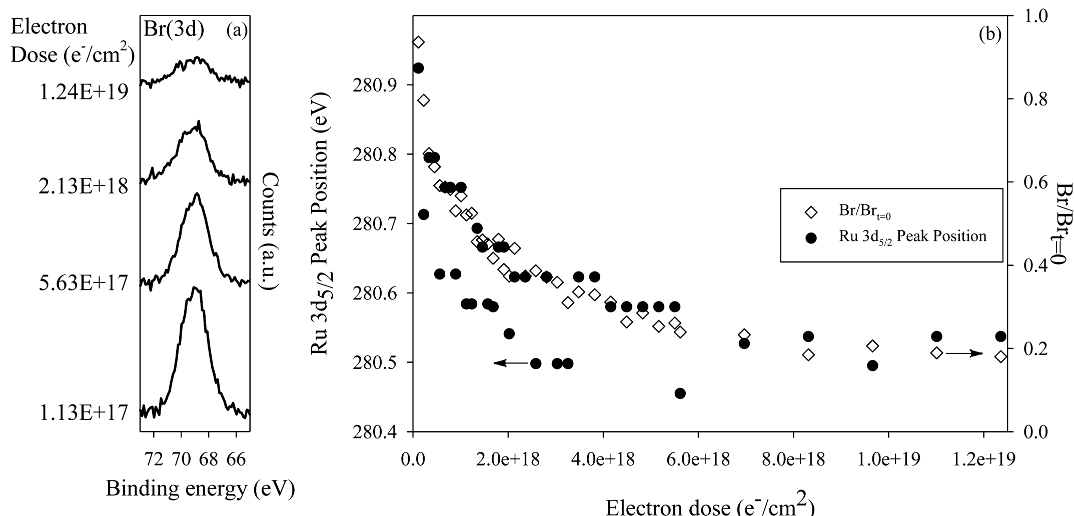

Figure 4. (a) Br(3d) XP region for an ~2 nm $[(\eta^3\text{-}C_3H_5)Ru(CO)_3Br]$ film exposed to electron doses ranging from 1.13×10^{17} to 1.24×10^{19} e^-/cm^2, and (b) changes in the fractional coverage of adsorbed bromine atoms (open diamonds) and the Ru $3d_{5/2}$ peak position (filled circles) for this film, plotted as a function of electron dose.

the Ru $3d_{5/2}$ binding energy correlated to the decrease in the Br(3d) peak area (Figure 4b). The effect of larger electron doses was, however, restricted to the loss of Br and the shift in Ru binding energy; there were no significant changes in the O(1s), C(1s), or Ru (3d) intensities.

Figure 5 shows a comparison of mass spectra of the neutral gas phase species produced when (a) *gas phase* $[(\eta^3\text{-}C_3H_5)Ru(CO)_3Br]$ molecules were exposed to 70 eV electrons, and (b) *adsorbed* $[(\eta^3\text{-}C_3H_5)Ru(CO)_3Br]$ molecules were irradiated by 500 eV electrons. In Figure 5a, fragmentation of gas phase $[(\eta^3\text{-}C_3H_5)Ru(CO)_3Br]$ molecules results in significant peaks for CO (m/z = 28), O (m/z = 16), C (m/z = 12), C_3H_n (n = 0−5, m/z = 36−41), C_2H_n (n = 0−3, m/z = 24−27), and CH_n (n = 0−3, m/z = 12−15) with smaller contributions from Br (m/z = 79, 81) and H_2O (m/z = 18, background species in the UHV chamber). In contrast to Figure 5a, Figure 5b is a much simpler mass spectrum with the presence of significant peaks for C (m/z = 12), O (m/z = 16), and CO (m/z = 28) with a minor peak corresponding to CH_2 (m/z = 14). Notably absent in Figure 5b are significant contributions from the C_3H_n and C_2H_n species observed in Figure 5a that are associated with the η^3-allyl group.

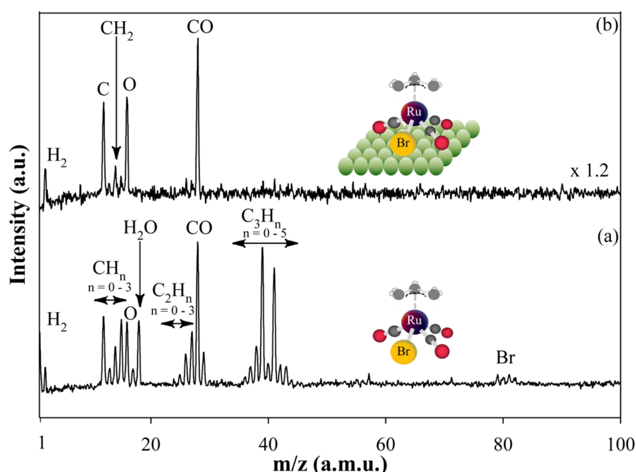

Figure 5. Mass spectrum (0−100 amu) of (a) the gas phase $[(\eta^3\text{-}C_3H_5)Ru(CO)_3Br]$ measured at $P_{[(\eta^3\text{-}C_3H_5)Ru(CO)_3Br]} \approx 1.5 \times 10^{-8}$ Torr, and (b) the volatile neutral species produced when an ~1.3 nm film of $[(\eta^3\text{-}C_3H_5)Ru(CO)_3Br]$, adsorbed onto a gold substrate at −168 °C, was irradiated by an electron dose of 1.13×10^{17} e^-/cm^2 (incident energy of 500 eV); the spectrum in (b) represents an average of MS taken every 20 s during the electron exposure. Spectrum (b) was normalized to the CO peak (m/z = 28).

Figure 6 shows how the rate of gas phase CO evolution measured by MS (open circles) and fractional coverage of the surface-bound oxygen species measured by XPS (filled triangles) change as a function of electron dose. The rate of CO evolution and corresponding change in the coverage of adsorbed oxygen atoms both decrease with increasing electron dose and follow a similar kinetic profile, decreasing to ~12% of their initial values after an electron dose of 3.74×10^{16} e^-/cm^2.

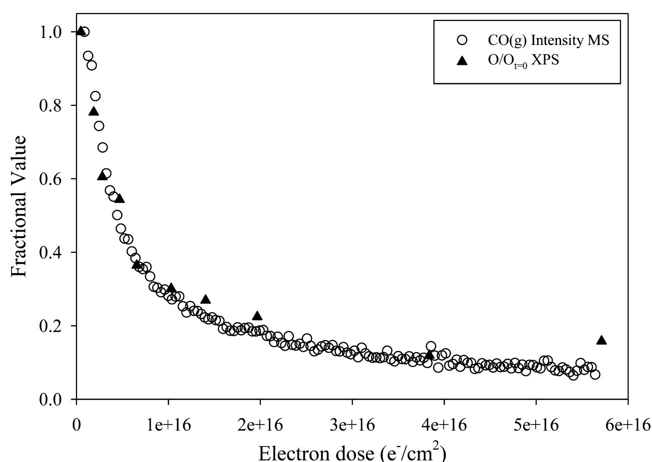

Figure 6. (open circles) Kinetics of gas phase CO (m/z = 28 amu) evolution from a $[(\eta^3\text{-}C_3H_5)Ru(CO)_3Br]$ film and (filled triangles) change in the fractional coverage of surface bound oxygen species ($O/O_{t=0}$). The fractional oxygen coverage was obtained by dividing the oxygen area by the initial oxygen area obtained by XPS.

Figure 7 provides data from a few selected experiments conducted with the chloride analogue, η^3-allyl ruthenium

DOI: 10.1021/acs.jpcc.5b03775
J. Phys. Chem. C 2015, 119, 15349−15359

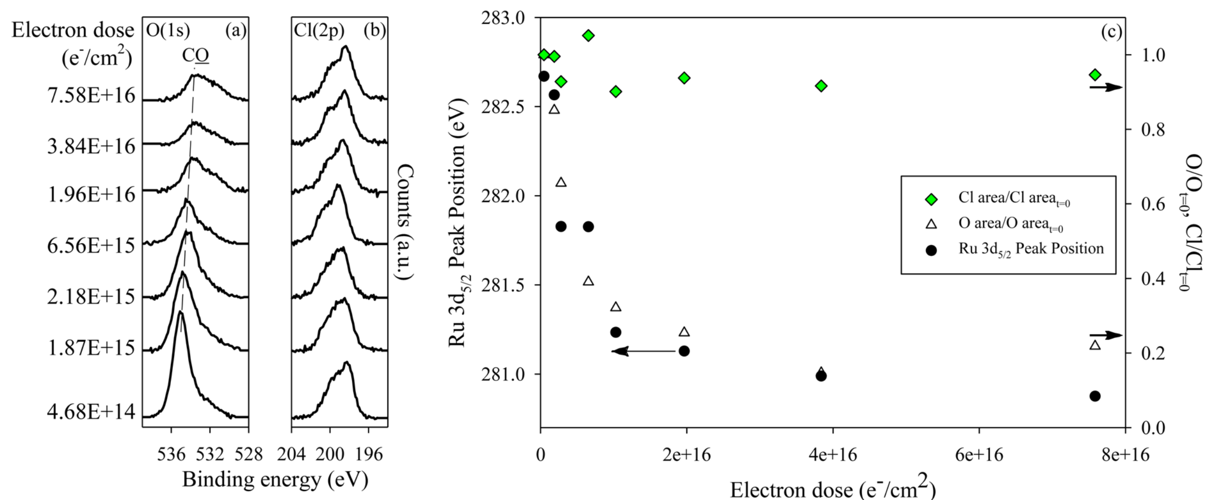

Figure 7. Evolution of the (a) O(1s) and (b) Cl(2p) XP regions for 1−2 nm thick films of $[(\eta^3\text{-}C_3H_5)Ru(CO)_3Cl]$ exposed to similar electron doses as seen for $[(\eta^3\text{-}C_3H_5)Ru(CO)_3Br]$ in Figure 1. (c) Changes in the fractional coverage of adsorbed oxygen and chlorine atoms and changes in Ru $3d_{5/2}$ binding energy for 1−2 nm $[(\eta^3\text{-}C_3H_5)Ru(CO)_3Cl]$ films plotted as a function of electron doses similar to those shown for $[(\eta^3\text{-}C_3H_5)Ru(CO)_3Br]$ in Figure 2. Films were adsorbed onto a:C at −168 °C, and spectra were normalized to account for slight differences in film thickness.

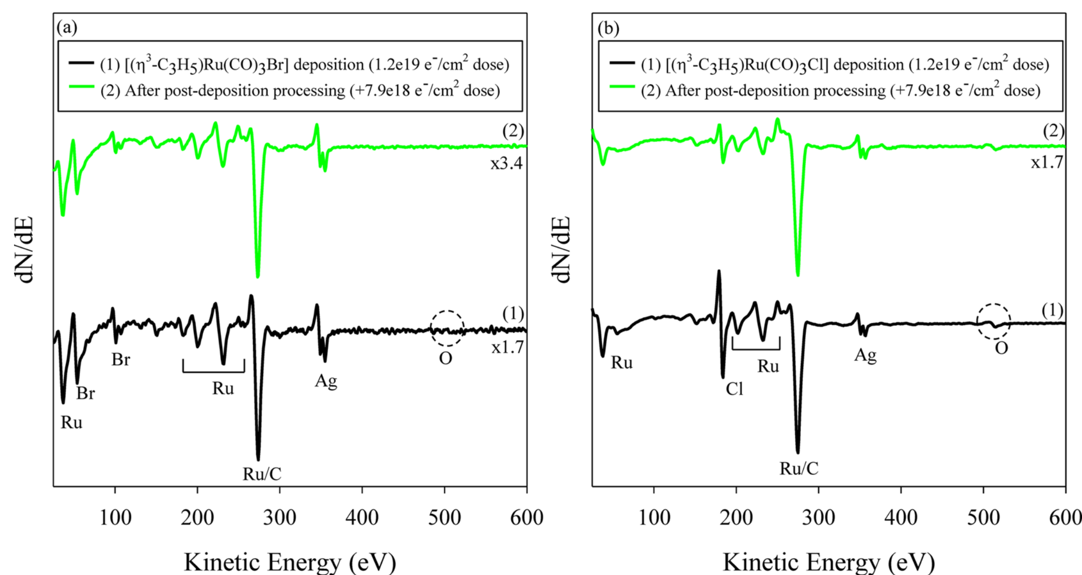

Figure 8. Auger electron spectra of EBID films created on an Ag substrate from (a) $[\eta^3\text{-}C_3H_5Ru(CO)_3Br]$ and (b) $[\eta^3\text{-}C_3H_5Ru(CO)_3Cl]$. In each case, the compound was deposited ((1), black line) and then subjected to further electron irradiation ((2), green line). Deposition conditions were $P_{[\eta^3\text{-}C_3H_5Ru(CO)_3Br/Cl]} \approx 5 \times 10^{-7}$ Torr, incident beam energy = 3 keV, and substrate current ≈ 700 nA for a total electron dose of (a)(1) 1.18×10^{19} e^-/cm^2, (a)(2) 2.06×10^{19} e^-/cm^2, (b)(1) 1.18×10^{19} e^-/cm^2, and (b)(2) 2.06×10^{19} e^-/cm^2. All AES were normalized to the Ru/C peak.

tricarbonyl chloride $[(\eta^3\text{-}C_3H_5)Ru(CO)_3Cl]$. Panels a and b in Figure 7 show the evolution of the O(1s) and Cl(2p) XPS regions, respectively, and Figure 7c displays changes in the O(1s) and Cl(2p) areas and in the Ru $3d_{5/2}$ binding energy, all plotted as a function of comparatively small electron doses ($\leq 7.58 \times 10^{16}$ e^-/cm^2). Figure 7a shows that the evolution of the O(1s) XPS region is similar to that observed for $[(\eta^3\text{-}C_3H_5)Ru(CO)_3Br]$ with a significant decrease in intensity and downshift in binding energy (compare Figure 7a with Figure 1). Similarly, the lack of change in the Cl(2p) region (<10% decrease after an electron dose of 7.58×10^{16} e^-/cm^2) is similar to the behavior of the Br(3d) region for $[(\eta^3\text{-}C_3H_5)Ru(CO)_3Br]$. Figure 7c demonstrates that, like Figure 2, the loss of oxygen from the film is also correlated with a decrease in the Ru $3d_{5/2}$ binding energy (Ru spectral data not shown). Thus, for both adsorbed $[(\eta^3\text{-}C_3H_5)Ru(CO)_3Cl]$ and $[(\eta^3\text{-}C_3H_5)Ru(CO)_3Br]$ films, an electron dose on the order of 1.0×10^{17} e^-/cm^2 results in a loss of >80% of the oxygen atoms and a decrease in the Ru $3d_{5/2}$ binding energy of ~1.7 eV with little or no change in the concentration of adsorbed halogen atoms.

Figure 8 shows Auger electron spectra (AES) for EBID deposits created on an Ag substrate under steady state deposition conditions. Figure 8a shows the AES of (1) a deposit created from $[(\eta^3\text{-}C_3H_5)Ru(CO)_3Br]$ and (2) the deposit subjected to post-deposition electron irradiation (i.e., post-deposition electron beam processing in the absence of any precursor molecules). Figure 8b shows analogous AES data for a deposition created from the Cl analogue $[(\eta^3\text{-}C_3H_5)Ru(CO)_3Cl]$. The AES data contained in Figure 8a(1) and b(1) show that the deposits are characterized by contributions from

DOI: 10.1021/acs.jpcc.5b03775
J. Phys. Chem. C 2015, 119, 15349−15359

Ru (273, 231, 200, 184, 176, 150 eV), C (272, 271 eV), and Br (108 eV) or Cl (181 eV) with essentially no contribution from O (503 eV). Thus, a comparison of Figures 1 and 8a shows that the chemical composition of the electron deposited films are similar with Ru, Br, and C but little or no evidence of O. A more quantitative analysis of the elemental composition of the deposits created in the AES was precluded, however, by the overlap between the principal Ru and C AES peaks at ~273 eV. Panels a(2) and b(2) in Figure 8 demonstrate that post-deposition electron beam processing produces a decrease in the concentration of adsorbed halogen atoms. This effect is more obvious for the $[(\eta^3\text{-}C_3H_5)Ru(CO)_3Cl]$ deposit due to the larger Cl peak present after deposition (Figure 8b(1)).

IV. DISCUSSION

XPS and MS data provided complementary information on the effect that electron exposure had on nanometer-thick films of $[(\eta^3\text{-}C_3H_5)Ru(CO)_3Br]$ and $[(\eta^3\text{-}C_3H_5)Ru(CO)_3Cl]$. This allowed for the correlation of changes in the chemical composition, bonding within the adsorbates, and the nature of the gas phase species. Experiments conducted in the AES instrument enabled data obtained on the chemical composition and effect of post-deposition electron beam processing to be compared between films created under low temperature, UHV conditions, and under steady state deposition conditions.

In summary, our XPS and MS data reveal that the surface reactions of adsorbed $[(\eta^3\text{-}C_3H_5)Ru(CO)_3Br]$ proceed in two stages. The initial step involves electron-stimulated precursor decomposition accompanied by the evolution of CO into the gas phase. However, under the influence of more prolonged electron beam irradiation, the film that forms as a result of $[(\eta^3\text{-}C_3H_5)Ru(CO)_3Br]$ decomposition loses Br atoms (step 2). This is the first example of an organometallic precursor we have studied where any ligand desorption has occurred after precursor decomposition. On the basis of previous studies and the similarity in the reactions induced by the 500 eV electrons and by X-ray irradiation (compare Figure 1 and Figures S3 and S4 in the Supporting Information) we believe that the reactions we observe are initiated by low energy secondary electrons (energies <100 eV) generated by interactions of the primary beam with the substrate reacting with the adsorbed species. The overall effect of electron irradiation on $[(\eta^3\text{-}C_3H_5)Ru(CO)_3Br]$ is shown in Scheme 1.

Stage 1: The initial stage of the reaction is complete after an electron dose of $\sim 1.12 \times 10^{17}$ e^-/cm^2 (see Figure 2). Experimentally, the decomposition of the $[(\eta^3\text{-}C_3H_5)Ru(CO)_3Br]$ precursor is most clearly evidenced by the decrease

Scheme 1. (Stage 1) Electron-Stimulated CO Desorption and $(\eta^3\text{-}C_3H_5)$ Decomposition from $[(\eta^3\text{-}C_3H_5)Ru(CO)_3Br]$; (Stage 2) Electron-Stimulated Desorption of Halogens from the Residual Product from Stage 1

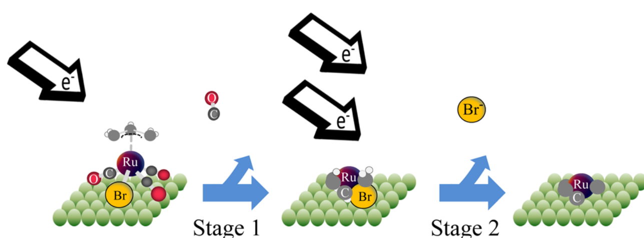

in binding energy of the Ru $3d_{5/2}$ peak from 282.8 to 280.9 eV as the Ru atoms are reduced from their initial +2 oxidation state. Analysis of Figures 5 and 6 indicates that it is also during this initial electron dose of $\sim 1.12 \times 10^{17}$ e^-/cm^2 that CO is evolved into the gas phase. Consistent with these observations, the CO peak, initially observed by XPS at ~288.5 eV (Figures 1 and 3) upon $[(\eta^3\text{-}C_3H_5)Ru(CO)_3Br]$ deposition, disappears for electron doses in excess of $\sim 1.13 \times 10^{17}$ e^-/cm^2. The ejection of CO into the gas phase is also responsible for the significant (>80%) decrease in the O(1s) signal intensity (see Figure 1), which is observed to follow the same dependence on electron dose as the rate of CO ejection (Figure 6) and the decrease in Ru $3d_{5/2}$ binding energy (Figure 2). It is possible that some of the oxygen loss occurs as a result of CO ligand decomposition and the ejection of a reactive oxygen species, such as O, O^-, or O^+ (CO(ads) → C(ads) + ROS(g)↑); this cannot be ruled out due to the inability to perform a quantitative analysis of the change in carbon atom concentration (resulting from the overlap with the Ru 3d peak as shown in Figure 3). However, on the basis of the correlation between the rate of CO evolved into the gas phase and the loss of oxygen from the adsorbate layer (Figure 6), we conclude that on average at least one of the original CO ligands is ejected as the molecular precursor decomposes. The loss of one or more CO ligands as a result of electron-stimulated reactions of surface-bound organometallics has been observed in related studies of other EBID precursors, notably $W(CO)_6$[32] and $Co(CO)_3(NO)$.[31]

In sharp contrast to the loss of CO, there is virtually no change in the Br(3d) signal intensity or binding energy (Figures 1 and 2) nor any evidence of Br desorption (Figure 5) as the precursor decomposes in stage 1. The lack of any measurable change in the Br binding energy suggests that the Ru−Br bond remains intact. Regarding the η^3-allyl $(\eta^3\text{-}C_3H_5)$ species, the mass spectrum shows no evidence of C_3H_n fragments being ejected during electron irradiation of surface-bound $[(\eta^3\text{-}C_3H_5)Ru(CO)_3Br]$, although these fragments are prominent in the mass spectrum of the gas phase $[(\eta^3\text{-}C_3H_5)Ru(CO)_3Br]$ (Figure 5). Although quantitative analysis of the C(1s) peak associated with the η^3-allyl $(\eta^3\text{-}C_3H_5)$ species is complicated by overlap with the larger Ru(3d) peaks (Figure 3), by conducting experiments on Au rather than a:C substrates, we can see that a residual C(1s) signal with a binding energy consistent with CC/CH species remains after electron irradiation. Moreover, the area of this peak is comparable to that ascribed to the three carbon atoms present in the η^3-allyl $(\eta^3\text{-}C_3H_5)$ ligand observed upon initial deposition (Figure 3). Thus, collectively, the MS and XPS data suggest that the carbon atoms in the η^3-allyl $(\eta^3\text{-}C_3H_5)$ ligand do not desorb as the precursor decomposes. This assertion is also consistent with the fate of other polyhapto unsaturated hydrocarbon ligands during electron irradiation of organometallic precursors, specifically η^5-cyclopentadienyl ligands $(\eta^5\text{-}C_5H_5)$, where all of the carbon atoms became trapped in the deposit.[28] Analysis of the Ru(3p) peak area (data not shown) indicates that electron irradiation does not cause any electron-stimulated desorption of the parent molecule.

Thus, the initial effect of electron irradiation is to decompose adsorbed $[(\eta^3\text{-}C_3H_5)Ru(CO)_3Br]$ molecules, causing ejection of at least one of the parent CO ligands while the Br atoms and the C atoms in the η^3-allyl $(\eta^3\text{-}C_3H_5)$ ligand are retained, although the η^3-allyl $(\eta^3\text{-}C_3H_5)$ ligand itself most likely decomposes. We believe that the inability of the polyhapto unsaturated hydrocarbon ligands, such as $\eta^3\text{-}C_3H_5$ (η^3-allyl) and

DOI: 10.1021/acs.jpcc.5b03775
J. Phys. Chem. C 2015, 119, 15349−15359

η^5-C_5H_5 ligands, to desorb during EBID is at least in part a consequence of their multidentate bonding to the central metal atom. Removal of an η^5-C_5H_5 ligand under standard solution conditions has been demonstrated to involve conversion first to an η^3-C_5H_5 ligand and then to a κ^1-C_5H_5 ligand before dissociation from the metal center.[37] As a result, multiple metal−ligand bonds must be broken, and the highly unsaturated and reactive fragments created must desorb from the surface before undergoing any secondary reactions. The chemical transformations described in stage 1, displayed pictorially in Scheme 1, cause the central metal atom to become reduced. The binding energy of the Ru atoms at the end of stage 1 (∼280.9 eV) is intermediate between their initial (+2) oxidation state (∼282.8 eV) in the [(η^3-C_3H_5)Ru$(CO)_3$Br] precursor and metallic Ru (279.9 ± 0.2 eV)[38−40] due to retention of the Ru−Br bond and encasement of Ru atoms in the carbonaceous matrix that is probably formed as the η^3-allyl ligand decomposes. Assuming that decomposition is initiated by a one electron process, a kinetic analysis based on the rate of decrease in the O(1s) signal as a function of electron dose (Figure 2) yields a total reaction cross-section for [(η^3-C_3H_5)Ru$(CO)_3$Br] decomposition ($\sigma_{[(C_3H_5Ru(CO)_3Br)]} \approx 5 \times 10^{-17}$ cm^2) with the 500 eV incident electrons used in this study, comparable to total reaction cross sections that have been calculated for other EBID precursors.[23,24,28] The similarity in the results observed for [(η^3-C_3H_5)Ru$(CO)_3$Cl] (compare Figures 1, 2, and 7) strongly supports the idea that the elementary reaction steps induced by electron irradiation are independent of the halogen atom's identity.

Stage 2: The second stage of the reaction (see Scheme 1) is characterized by a loss of Br atoms from the film (shown in Figure 4) postulated to be a result of an electron-stimulated desorption (ESD) type process[41−43] that can be written in its most general form as

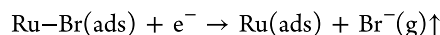

$$\text{Ru–Br(ads)} + e^- \rightarrow \text{Ru(ads)} + \text{Br}^-\text{(g)}\uparrow$$

The cleavage of Ru−Br bonds, and the loss of bromine atoms from the film, is responsible for the closely correlated and systematic decrease in the Ru $3d_{5/2}$ peak position, as shown in Figure 4. In contrast to the electron-stimulated decomposition of the parent molecule (stage 1), which is complete within an electron dose of $\sim 1.13 \times 10^{17}$ e^-/cm^2, the loss of measurable (>10%) amounts of Br requires electron doses of $>5 \times 10^{17}$ e^-/cm^2, indicating a slower and less efficient process. Indeed, the small (<10%) loss of Br atoms observed in Figure 2 for electron doses $<1.13 \times 10^{17}$ e^-/cm^2 represents the beginning of the ESD process, which in reality begins as soon as the precursor has undergone decomposition, although its importance only becomes truly apparent for the much larger electron doses ($>1.13 \times 10^{17}$ e^-/cm^2), as shown in Figure 4. Aside from the loss of Br and its effect on the binding energy of the Ru atoms, no other chemical transformations occur during this second stage of the reaction. Figure 6 shows that there is no CO evolution, and there are also no significant changes to the oxygen or carbon concentrations as measured by XPS (data not shown). The overall effect of electron irradiation is shown in Scheme 1.

Comparisons to Related Studies. Previous studies on the electron-stimulated reactions of surface bound organometallics have identified two sequential steps that occur as a function of increasing electron dose: precursor decomposition accompanied by ligand desorption followed by electron-induced decomposition of residual ligands. In the present study, the first step is also characterized by decomposition of the parent [(η^3-C_3H_5)Ru$(CO)_3$Br] compound accompanied by CO (ligand) desorption. Moreover, a comparison between the reactions of [(η^3-C_3H_5)Ru$(CO)_3$Br] and $Co(CO)_3(NO)$[31] reveals that, for both molecules, decomposition of the parent leads exclusively to the ejection of CO groups, which appears to be a "preferred leaving group" in these electron stimulated reactions. In the present study, there is also no evidence of significant Br loss during precursor decomposition, consistent with recent gas phase studies on the interactions of low energy (<100 eV) electrons with [(η^3-C_3H_5)Ru$(CO)_3$Br](g).[44] This lack of Ru−Br bond cleavage during the electron-stimulated decomposition of [(η^3-C_3H_5)Ru$(CO)_3$Br] is perhaps somewhat surprising given the high electron affinity of halide ions.

The most notable and significant difference between the electron-stimulated reactions of adsorbed [(η^3-C_3H_5)Ru$(CO)_3$Br] molecules and other organometallic precursors studied to date occurs in the second stage of the reaction (step 2), which has been previously characterized exclusively by ligand decomposition. For example, in the case of $W(CO)_6$,[32] electron-stimulated reactions of the partially decarbonylated species ($W_x(CO)_y$) left behind after ejection of multiple CO ligands in the initial step leads to CO decomposition as follows

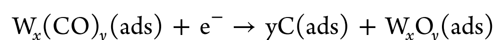

$$W_x(CO)_y\text{(ads)} + e^- \rightarrow y\text{C(ads)} + W_xO_y\text{(ads)}$$

It is this second step that we believe is responsible for most of the unwanted organic contamination prevalent in many EBID deposits created from organometallic precursors. In contrast, the second stage in the electron-stimulated reactions of adsorbed [(η^3-C_3H_5)Ru$(CO)_3$Br] molecules is characterized not by ligand decomposition but by Br atom desorption; after a total electron dose of $>1.13 \times 10^{19}$ e^-/cm^2, ∼80% of the Br atoms have been removed from the film (Figure 4). Thus, although the halogen atoms are not removed initially as the [(η^3-C_3H_5)Ru$(CO)_3$Br] molecules undergo electron-stimulated decomposition, they can be removed from the resulting film that forms via a slower electron-stimulated desorption (ESD) process.

Relevance to Electron Beam-Induced Deposition Experiments. The UHV surface science studies discussed in Figures 1−7 pertain to the electron-stimulated reactions experienced by thin films of precursor molecules adsorbed at low temperatures (<150 K). In contrast, the films created in the Auger electron spectrometer (Figure 8) are generated under steady state deposition conditions, much more representative of those used in typical EBID experiments, where a sample at room temperature is continuously irradiated by an electron beam in the presence of a constant partial pressure of precursor molecules.[1−4] Consequently, the AES data in Figure 8 can be used to gauge the extent to which data from the UHV surface science studies can inform and provide insights on the chemical composition of EBID structures. A comparison of Figures 1 and 8 reveals that the chemical composition of the films created by electron irradiation under UHV conditions (Figures 1) and in the AES (Figure 8) are similar with evidence of Ru, Br, and C but little or no evidence of O in the deposits. Moreover, post-deposition electron irradiation of the deposits created in the AES decreases the halogen atom concentration in accordance with the data shown in Figure 4. These similarities support the idea that the same sequence of fundamental bond breaking processes identified in the low temperature UHV studies is also operative during EBID. The electron flux in the AES

DOI: 10.1021/acs.jpcc.5b03775
J. Phys. Chem. C 2015, 119, 15349−15359

experiments is greater than the highest electron fluxes used in the UHV surface science studies, so at first glance it appears surprising that there are any residual halogen atoms in the deposits. However, under the steady state deposition conditions that characterize the AES experiments, electron beam processing of the deposits, which would lead to removal of halogen atoms via an ESD process, must compete with electron-stimulated deposition involving reactions of constantly adsorbing precursor molecules. Under conditions where the deposition rate is greater than the rate of electron beam processing, residual halogen atoms will not desorb but will instead become incorporated into the growing film. However, in the absence of any background partial pressure of precursor molecules, growth ceases and halogen atoms will be more susceptible to removal by post-deposition electron beam processing. This qualitatively explains the observations shown in Figure 8. Indeed, this argument also suggests that the metal concentration in EBID films created from [(η^3-C_3H_5)Ru-$(CO)_3$Br] will be enhanced under so-called "precursor-limited" deposition conditions, where the growth rate is limited by the concentration of adsorbed precursor molecules. Under these growth conditions, the products of the initial precursor decomposition step (stage 1) will be subject to extensive post-deposition electron beam processing prior to the next deposition event. As can be seen from the UHV surface science studies, this will promote halogen desorption and thus improve the final metal concentration in the deposit.

The similarity in the electron-stimulated reactions of [(η^3-C_3H_5)Ru$(CO)_3$Br] and [(η^3-C_3H_5)Ru$(CO)_3$Cl] also has implications for EBID. On one hand, it is desirable to have precursors that are volatile at room temperature and therefore easier to handle. Organometallic precursors that contain metal−chlorine bonds are typically more volatile than those that contain metal−bromine bonds due to weaker intermolecular forces and lower molecular weight.[45] This was reflected in the relative volatilities observed for [(η^3-C_3H_5)Ru$(CO)_3$Br] and [(η^3-C_3H_5)Ru$(CO)_3$Cl]. Consequently, the similar results obtained for these two precursors suggest that the chemical identity of halogen atoms in organometallic complexes can be tuned to optimize volatility and stability during volatilization and transport without changing the fundamental bond breaking steps involved in EBID. As pointed out recently by Mulders,[13] however, another factor that must be considered in selecting EBID precursors is the potential for unwanted reactions of byproducts formed as a result of ligand decomposition. This includes halogen atoms that can etch Si, often used as the substrate in EBID. In this respect, [(η^3-C_3H_5)Ru$(CO)_3$Br] would be preferred over [(η^3-C_3H_5)Ru$(CO)_3$Cl] because Br is far less efficient at etching Si or the native oxide layer typically present on Si surfaces as compared to Cl.[46,47]

Finally, it should be noted that the findings from the present study, notably the preferential ejection of CO ligands in the precursor decomposition step (stage 1), coupled with the ability of post-deposition electron beam processing to remove adsorbed halogen atoms (stage 2), may help to explain why ClAuCO has been used to deposit pure Au nanostructures using EBID via the following reaction sequence.[48]

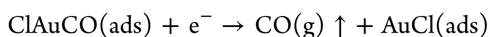

$$\mathrm{ClAuCO(ads)} + e^- \rightarrow \mathrm{CO(g)}\uparrow + \mathrm{AuCl(ads)}$$

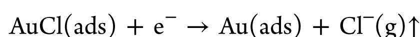

$$\mathrm{AuCl(ads)} + e^- \rightarrow \mathrm{Au(ads)} + \mathrm{Cl^-(g)}\uparrow$$

V. CONCLUSIONS

Surface bound η^3-allyl ruthenium tricarbonyl bromide [(η^3-C_3H_5)Ru$(CO)_3$Br] molecules are decomposed by electron irradiation in a process that initially reduces the central metal (Ru) atoms and ejects CO ligands into the gas phase, and the carbon atoms contained within the η^3-allyl (η^3-C_3H_5) ligand are incorporated into the metal-containing deposit that forms. In the second step that occurs for significantly larger electron doses, most of the bromine atoms are removed from the deposits via an electron-stimulated desorption process, analogous to a post-deposition electron-beam processing step. The electron-stimulated reactions of the organometallic precursors appear invariant to the nature of the halogen atom. Considered collectively, results from this investigation suggest that by using organometallic precursors that contain a small number of CO ligands and/or metal−halogen bonds, EBID could create deposits with higher metal percentages under precursor-limited deposition conditions. This assertion is consistent with previous studies where pure Au nanostructures have been deposited by EBID from ClAuCO.[48]

■ ASSOCIATED CONTENT

Supporting Information

Effect of heating [(η^3-C_3H_5)Ru$(CO)_3$Br] on the deposit formed on a Au substrate (Figure S1); Attenuated Total Reflectance (ATR) Infrared spectra for (a) [(η^3-C_3H_5)Ru-$(CO)_3$Br] (b) [(η^3-C_3H_5)Ru$(CO)_3$Cl] (Figure S2); Effect of X-ray Irradiation on a ~ 1.6 nm thick film of [(η^3-C_3H_5)Ru$(CO)_3$Br] adsorbed on Au (Figure S3); Effect of X-ray Irradiation on a ~ 1.6 nm thick film of [(η^3-C_3H_5)Ru-$(CO)_3$Br] adsorbed on HOPG (Figure S4) The Supporting Information is available free of charge on the ACS Publications website at DOI: 10.1021/acs.jpcc.5b03775.

■ AUTHOR INFORMATION

Corresponding Author

*E-mail: howardf@jhu.edu.

Notes

The authors declare no competing financial interest.

■ ACKNOWLEDGMENTS

D.H.F. and L.M.W. thank the donors of the American Chemical Society Petroleum Research Fund for support of this work (PRF Grant # 54519-ND5).

■ REFERENCES

(1) Huth, M.; Porrati, F.; Schwalb, C.; Winhold, M.; Sachser, R.; Dukic, M.; Adams, J.; Fantner, G. Focused Electron Beam Induced Deposition: A Perspective. *Beilstein J. Nanotechnol.* **2012**, *3*, 597−619.
(2) Randolph, S.; Fowlkes, J.; Rack, P. Focused, Nanoscale Electron-beam-induced Deposition and Etching. *Crit. Rev. Solid State Mater. Sci.* **2006**, *31*, 55−89.
(3) Utke, I.; Hoffmann, P.; Melngailis, J. Gas-assisted Focused Electron Beam and Ion Beam Processing and Fabrication. *J. Vac. Sci. Technol., B* **2008**, *26*, 1197−1276.
(4) van Dorp, W.; Hagen, C. A Critical Literature Review of Focused Electron Beam Induced Deposition. *J. Appl. Phys.* **2008**, *104*, 081301.
(5) van Dorp, W. Sub-10 nm Writing: Focused Electron Beam-induced Deposition in Perspective. *Appl. Phys. A: Mater. Sci. Process.* **2014**, *117*, 1615−1622.
(6) van Dorp, W.; Hagen, C.; Crozier, P.; Kruit, P. Growth Behavior Near the Ultimate Resolution of Nanometer-scale Focused Electron Beam-induced Deposition. *Nanotechnology* **2008**, *19*, 225305.

DOI: 10.1021/acs.jpcc.5b03775
J. Phys. Chem. C 2015, 119, 15349−15359

(7) Edinger, K.; Becht, H.; Bihr, J.; Boegli, V.; Budach, M.; Hofmann, T.; Koops, H. W.; Kuschnerus, P.; Oster, J.; Spies, P. Electron-beam-based Photomask Repair. *J. Vac. Sci. Technol., B* **2004**, *22*, 2902−2906.
(8) Heerkens, C. T. H.; Kamerbeek, M.; van Dorp, W.; Hagen, C.; Hoekstra, J. Electron Beam Induced Deposited Etch Masks. *Microelectron. Eng.* **2009**, *86*, 961−964.
(9) Liang, T.; Frendberg, E.; Lieberman, B.; Stivers, A. Advanced Photolithographic Mask Repair Using Electron Beams. *J. Vac. Sci. Technol., B* **2005**, *23*, 3101−3105.
(10) Hübner, B.; Koops, H.; Pagnia, H.; Sotnik, N.; Urban, J.; Weber, M. Tips for Scanning Tunneling Microscopy Produced by Electron-beam-induced Deposition. *Ultramicroscopy* **1992**, *42*, 1519−1525.
(11) Brown, J.; Kocher, P.; Ramanujan, C. S.; Sharp, D. N.; Torimitsu, K.; Ryan, J. F. Electrically Conducting, Ultra-sharp, High Aspect-ratio Probes for AFM Fabricated by Electron-beam-induced Deposition of Platinum. *Ultramicroscopy* **2013**, *133*, 62−66.
(12) Chen, I.-C.; Chen, L.-H.; Ye, X.-R.; Daraio, C.; Jin, S.; Orme, C. A.; Quist, A.; Lal, R. Extremely Sharp Carbon Nanocone Probes for Atomic Force Microscopy Imaging. *Appl. Phys. Lett.* **2006**, *88*, 153102.
(13) Mulders, J. Practical Precursor Aspects for Electron Beam Induced Deposition. *Nanofabrication* **2014**, *1*, 74−79.
(14) Botman, A.; Hesselberth, M.; Mulders, J. Improving the Conductivity of Platinum-Containing Nano-structures Created by Electron-beam-induced Deposition. *Microelectron. Eng.* **2008**, *85*, 1139−1142.
(15) van Dorp, W. F.; Wu, X.; Mulders, J. J. L.; Harder, S.; Rudolf, P.; De Hosson, J. Gold Complexes for Focused-Electron-Beam-Induced Deposition. *Langmuir* **2014**, *30*, 12097−12105.
(16) Engmann, S.; Stano, M.; Matejc, S.; Ingolfsson, O. Gas Phase Low Energy Electron Induced Decomposition of the Focused Electron Beam Induced Deposition (FEBID) Precursor Trimethyl (Methyl-cyclopentadienyl) Platinum(IV) ($MeCpPtMe_3$). *Phys. Chem. Chem. Phys.* **2012**, *14*, 14611−14618.
(17) Engmann, S.; Stano, M.; Matejcik, S.; Ingolfsson, O. The Role of Dissociative Electron Attachment in Focused Electron Beam Induced Processing: A Case Study on Cobalt Tricarbonyl Nitrosyl. *Angew. Chem., Int. Ed.* **2011**, *50*, 9475−9477.
(18) Engmann, S.; Stano, M.; Papp, P.; Brunger, M. J.; Matejcik, S.; Ingolfsson, O. Absolute Cross Sections for Dissociative Electron Attachment and Dissociative Ionization of Cobalt Tricarbonyl Nitrosyl in the Energy Range from 0 to 140 eV. *J. Chem. Phys.* **2013**, *138*, 044305/1−044305/7.
(19) Wnorowski, K.; Stano, M.; Barszczewska, W.; Jówko, A.; Matejčík, Š. Electron Ionization of $W(CO)_6$: Appearance Energies. *Int. J. Mass Spectrom.* **2012**, *314*, 42−48.
(20) Wnorowski, K.; Stano, M.; Matias, C.; Denifl, S.; Barszczewska, W.; Matejčík, Š. Low-energy Electron Interactions with Tungsten Hexacarbonyl - $W(CO)_6$. *Rapid Commun. Mass Spectrom.* **2012**, *26*, 1−6.
(21) Bishop, J.; Lobo, C. J.; Martin, A.; Ford, M.; Phillips, M.; Toth, M. Role of Activated Chemisorption in Gas-Mediated Electron Beam Induced Deposition. *Phys. Rev. Lett.* **2012**, *109*, 146103.
(22) Martin, A. A.; Phillips, M. R.; Toth, M. Dynamic Surface Site Activation: A Rate Limiting Process in Electron Beam Induced Etching. *ACS Appl. Mater. Interfaces* **2013**, *5*, 8002−8007.
(23) van Dorp, W. F.; Wnuk, J. D.; Gorham, J. M.; Fairbrother, D. H.; Madey, T. E.; Hagen, C. W. Electron Induced Dissociation of Trimethyl, Methylcyclopentadienyl Platinum, IV: Total Cross Section as a Function of Incident Electron Energy. *J. Appl. Phys.* **2009**, *106*, 074903.
(24) Landheer, K.; Rosenberg, S. G.; Bernau, L.; Swiderek, P.; Utke, I.; Hagen, C. W.; Fairbrother, D. H. Low-Energy Electron-Induced Decomposition and Reactions of Adsorbed Tetrakis (Trifluorophosphine) Platinum $[Pt(PF_3)_4]$. *J. Phys. Chem. C* **2011**, *115*, 17452−17463.
(25) Rosenberg, S. G.; Landheer, K.; Hagen, C. W.; Fairbrother, D. H. Substrate Temperature and Electron Fluence Effects on Metallic Films Created by Electron Beam Induced Deposition. *J. Vac. Sci. Technol., B* **2012**, *30*, 051805.
(26) Spencer, J. A.; Rosenberg, S. G.; Barclay, M.; Wu, Y.-C.; McElwee-White, L.; Fairbrother, D. H. Understanding the Electron-stimulated Surface Reactions of Organometallic Complexes to Enable Design of Precursors for Electron Beam-induced Deposition. *Appl. Phys. A: Mater. Sci. Process.* **2014**, *117*, 1631−1644.
(27) Wnuk, J.; Rosenberg, S.; Gorham, J.; van Dorp, W.; Hagen, C.; Fairbrother, D. Electron Beam Deposition for Nanofabrication: Insights from Surface Science. *Surf. Sci.* **2011**, *605*, 257−266.
(28) Wnuk, J. D.; Gorham, J. M.; Rosenberg, S. G.; van Dorp, W. F.; Madey, T. E.; Hagen, C. W.; Fairbrother, D. H. Electron Induced Surface Reactions of the Organometallic Precursor Trimethyl (Methylcyclopentadienyl) Platinum (IV). *J. Phys. Chem. C* **2009**, *113*, 2487−2496.
(29) Hedhili, M. N.; Bredehöft, J. H.; Swiderek, P. Electron-induced Reactions of $MeCpPtMe_3$ Investigated by HREELS. *J. Phys. Chem. C* **2009**, *113*, 13282−13286.
(30) Warneke, J.; van Dorp, W.; Rudolf, P.; Stano, M.; Papp, P.; Matejcik, S.; Borrmann, T.; Swiderek, P. Acetone and the Precursor Ligand Acetylacetone: Distinctly Different Electron Beam Induced Decomposition? *Phys. Chem. Chem. Phys.* **2015**, *17*, 1204−1216.
(31) Rosenberg, S. G.; Barclay, M.; Fairbrother, D. H. Electron Beam Induced Reactions of Adsorbed Cobalt Tricarbonyl Nitrosyl ($Co(CO)_3NO$) Molecules. *J. Phys. Chem. C* **2013**, *117*, 16053−16064.
(32) Rosenberg, S. G.; Barclay, M.; Fairbrother, D. H. Electron Induced Reactions of Surface Adsorbed Tungsten Hexacarbonyl ($W(CO)_6$. *Phys. Chem. Chem. Phys.* **2013**, *15*, 4002−4015.
(33) Rosenberg, S. G.; Barclay, M.; Fairbrother, D. H. Electron Induced Surface Reactions of Organometallic Metal $(hfac)_2$ Precursors and Deposit Purification. *ACS Appl. Mater. Interfaces* **2014**, *6*, 8590−8601.
(34) Wnuk, J. D.; Gorham, J. M.; Rosenberg, S. G.; van Dorp, W. F.; Madey, T. E.; Hagen, C. W.; Fairbrother, D. H. Electron Beam Irradiation of Dimethyl-(acetylacetonate) Gold (III) Adsorbed onto Solid Substrates. *J. Appl. Phys.* **2010**, *107*, 054301.
(35) Sbrana, G.; Braca, G.; Piacenti, F.; Pino, P. Synthesis of π-Allylruthenium Tricarbonyl Halides. *J. Organomet. Chem.* **1968**, *13*, 240−242.
(36) Moulder, J. F.; Stickle, W. F.; Sobol, P. E.; Bomben, K. D. *Handbook of X-ray Photoelectron Spectroscopy*; Physical Electronics USA, Inc.: Chanhassen, Minnesota, USA, 1995.
(37) Casey, C. P.; O'Connor, J. M.; Haller, K. J. Interconversion of η^5-C_5H_5, η^1-C_5H_5, and Ionic "η^0"-C_5H_5 Rhenium Compounds-X-ray Crystal Structure of $[Re(NO)(CH_3)(PMe_3)_4]^+[C_5H_5]^-$. *J. Am. Chem. Soc.* **1985**, *107*, 1241−1246.
(38) Fuggle, J. C.; Madey, T. E.; Steinkilberg, M.; Menzel, D. Photoelectron Spectroscopic Studies of Adsorption of CO and Oxygen on Ru(001). *Surf. Sci.* **1975**, *52*, 521−541.
(39) Kim, K. S.; Winograd, N. X-Ray Photoelectron Spectroscopic Studies of Ruthenium-Oxygen Surfaces. *J. Catal.* **1974**, *35*, 66−72.
(40) Shen, J. Y.; Adnot, A.; Kaliaguine, S. An ESCA Study of the Interaction of Oxygen with the Surface of Ruthenium. *Appl. Surf. Sci.* **1991**, *51*, 47−60.
(41) Tegeder, P.; Smirnov, B. M.; Illenberger, E. Electron Stimulated Desorption from Molecules on a Noble Gas Solid: An Analysis of Cluster and Island Formation Upon Deposition. *Int. J. Mass Spectrom.* **2001**, *205*, 331−337.
(42) Trenhaile, B. R.; Antonov, V. N.; Xu, G. J.; Agrawal, A.; Signor, A. W.; Butera, R. E.; Nakayama, K. S.; Weaver, J. H. Phonon-activated Electron-stimulated Desorption of Halogens from Si(100)-(2 × 1). *Phys. Rev. B* **2006**, *73*, 125318/1−125318/8.
(43) Walter, W. K.; Jones, R. G. Chlorine Adsorption on Cu(111) - Low-Temperature Adsorption, Electron-Stimulated Desorption and Chloride Formation. *J. Phys.: Condens. Matter* **1989**, *1*, SB201−SB202.
(44) Thorman, R.; Ómarsson, B.; Ingólfsson, O. Low energy election induced decomposition of gas phase η^3-allyl ruthenium tricarbonyl bromide, a potential focused election beam induced deposition (FEBID) precursor. To be submitted for publication.
(45) Boxhoorn, G.; Jesse, A. C.; Ernsting, J. M.; Oskam, A. Vapor Pressure Measurements on $M(CO)_5PX_3$ (M = Chromium, Molybde-

num, Tungsten, X = Fluorine, Chlorine, Bromine). *Thermochim. Acta* **1978**, *27*, 261−267.

(46) Bestwick, T. D.; Oehrlein, G. S. Reactive Ion Etching of Silicon using Bromine Containing Plasmas. *J. Vac. Sci. Technol. A* **1990**, *8*, 1698−1701.

(47) Reinicke, M. *Investigation of Physical and Chemical Interactions During Etching of Silicon in Dual Frequency Capacitively Coupled HBr/NF_3 Gas Discharges*; Books on Demand Gmbh, 2009.

(48) Mulders, J.; Veerhoek, J.; Bosch, E.; Trompenaars, P. Fabrication of Pure Gold Nanostructures by Electron Beam Induced Deposition with Au (CO)Cl Precursor: Deposition Characteristics and Primary Beam Scattering Effects. *J. Phys. D: Appl. Phys.* **2012**, *45*, 475301.

DOI: 10.1021/acs.jpcc.5b03775
J. Phys. Chem. C 2015, 119, 15349−15359